J. Fluid Mech. (1983), *vol.* 126, *pp.* 269–285
Printed in Great Britain

Flow in a differentially rotated cylindrical drop at low Reynolds number

By GEORGE M. HARRIOTT AND ROBERT A. BROWN
Department of Chemical Engineering, Massachusetts Institute of Technology, Cambridge, Massachusetts 02139

(Received 4 May 1982)

A liquid drop held captive between parallel disks that are differentially rotated is a model for the swirling flows induced by crystal rotation in the floating-zone process for growing semiconductor materials. An asymptotic analysis for a cylindrical drop is presented that elucidates the structure of the axisymmetric cellular motions caused by disk rotation at low Reynolds number. Variations of meniscus shape induced by these flows are described in the limit of small capillary number. Most cellular flow fields break the bifurcation point that corresponds to the Plateau–Rayleigh limit for the length of a static drop into two disjoint shape families and lower the maximum stable drop length. This effect is studied by a singular bifurcation analysis.

1. Introduction

A liquid drop that forms a bridge between two coaxial and parallel solid surfaces is a fluid-mechanical model of the floating-zone process for growing semiconductor materials of high purity (Carruthers & Grasso 1972; Fowle *et al.* 1980). Here a cylindrical rod of a multicomponent and polycrystalline material is melted and resolidified into a single crystal by using a short circumferential heater that translates slowly along the axis of the rod. The molten zone forms between the crystal and feed rods and is held in place by surface tension. Its size is governed by heat transfer and limited by instabilities that originate at the melt/gas meniscus. In practice, the radius of the rods and the height of the zone range roughly between 0·5 and 3 cm.

Achieving a high degree of uniformity in the product crystal requires suppression of the azimuthal variations in the thermal field, caused by imperfect heater design, and promotion of the uniform transfer of solutes from the melt to the solidification interface. Azimuthal variations of the thermal field are moderated by rotating the feed and crystal rods that bound the melt; for this purpose solid-body rotation would suffice. Yet differential rotation of these rods is a common practice, for the cellular flows that result are believed to smooth the radial distribution of solute across the growing interface.

The only theories for composition variation that account for the flows induced by rotation (Burton, Prim & Slichter 1953) treat the crystal surface as an infinite rotating disk and use fluid mechanics based on the similarity solution that is available in this limit (Cochran 1934). The radial turning flows, which are ignored in the infinite-disk analysis, play a large role in setting the dopant distribution across the crystal, especially in the small-scale growth systems that are used in laboratories and are being designed for experiments in outer space. The multicellular structure of these flows has been noted experimentally in a model system (Fowle *et al.* 1980).

In this report we present asymptotic results for the structure of these swirling flows

and the interaction between these flows and the shape of the meniscus in the limit of low rotation rates, as measured by the Reynolds number, of a nearly cylindrical liquid zone. The slow translation rate of the melt through the rod is ignored and the zone is modelled as being stationary between two circular solid disks; this model is precisely the one used in the experiments of Fowle *et al.* (1980). The formulation of the free-boundary problem for the flow and meniscus shape is presented in §2, along with a solution scheme for almost-cylindrical zones of melts with low capillary numbers. The cellular flow fields for zero capillary number are analysed in §3 in the limit of small Reynolds number, and the meniscus deformations caused by these flows are presented in §4.

The limits of stability of a captive liquid zone have been laid out in the cases where the liquid is either hydrostatic or gyrostatic (Heywang 1956; Coriell, Hardy & Cordes 1977; Boucher & Evans 1980; Brown & Scriven 1980; Ungar & Brown 1982). It has long been known (Plateau 1873; Rayleigh 1879; Mason 1970) that the height of a static cylindrical drop cannot exceed its perimeter; drops with a greater length will reduce their surface energy by becoming unduloidally shaped and will eventually break up into droplets. An alternative way of viewing this stability limit comes from studying the possibility of multiple equilibrium shapes of the static zone. In this context, the Plateau–Rayleigh limit for the drop length is denoted by the bifurcation of a family of equilibrium unduloidal menisci from the perfectly cylindrical forms (Mason 1970; Ungar & Brown 1982).

Each unduloidal shape is reflectively antisymmetric about a plane perpendicular to the axis of rotation and halfway between the two disks. The shapes bulge out near one disk and neck in at the other to conserve volume. There are two distinct shape families of unduloids because, in the absence of gravity, the orientation of the meniscus is arbitrary. The families of unduloids evolve toward lengths shorter than the stability limit and are unstable.

The effects of gravity, drop volume and rigid rotation on meniscus stability have been described as changes in the bifurcation point that represents the Plateau–Rayleigh limit (Brown & Scriven 1980; Ungar & Brown 1982). The symmetry of the change in the cylindrical meniscus caused by varying any of these parameters sets the qualitative behaviour for the change of the bifurcation point. When the meniscus deflection is reflectively symmetric about the midplane, variation of the new parameter couples weakly into the bifurcation behaviour. Parameters that lead to antisymmetric meniscus deflections catastrophically change the structure of the shape families near the Plateau–Rayleigh limit by rupturing the bifurcation point into two separate shape families; the new limit of stability is marked by a maximum drop length where the family of stable shapes turns back to shorter drops and loses stability. The value of the maximum drop length is quite sensitive to changes in the parameter.

The interaction between the cellular flows induced by differential rotation and the Plateau–Rayleigh limit is also governed by the symmetry of the meniscus deflection caused by the flow field. As shown below, these deflections are generally not reflectively symmetric and so rupture the structure of the shape families as described above. This result is laid out mathematically in §4 by application of the singular perturbation techniques developed by Matkowsky & Reiss (1977) for studying imperfect bifuractions.

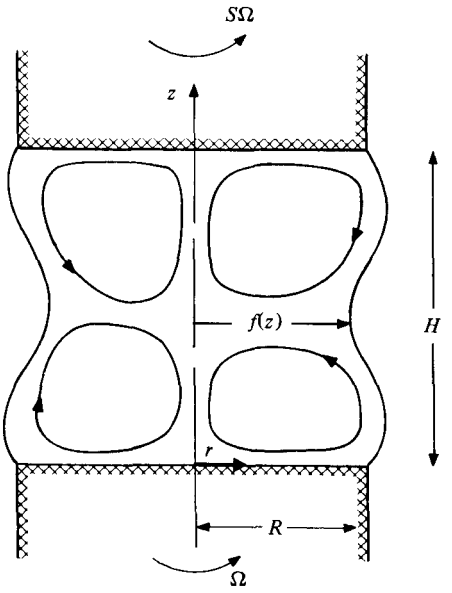

FIGURE 1. A differentially rotated cylindrical drop with radius R and height H.

2. Formulation

We consider a weightless and isothermal drop of a Newtonian liquid held between two circular solid surfaces of radius R that are separated by a distance H, as shown in figure 1. The drop shape and the flow inside are represented in a stationary dimensionless cylindrical coordinate system defined by scaling axial distances with H and radial distances with R. The drop is assumed to have the volume of the cylinder that meets the edges of the solid faces where the meniscus pins. This is the appropriate contact condition for a melt/solid system in a floating zone without translation and for the model experiments of Fowle *et al.* (1980) so long as the Gibbs criterion (Gibbs 1906; Lawal & Brown 1982) for the apparent contact angle is met.

Axisymmetric flows are induced by rotating the lower face at speed Ω and the top at $s\Omega$, and influence the shape of the meniscus, which is represented by the dimensionless radial function $f(z)$. The local orientation of the meniscus is given by the unit normal

$$\mathbf{n} \equiv \frac{\mathbf{e}_r - \Lambda f'(z)\mathbf{e}_z}{(1+\Lambda^2 f'(z)^2)^{\frac{1}{2}}} \tag{1}$$

and the tangent vectors

$$\mathbf{t}_\theta \equiv f(z)\,\mathbf{e}_\theta, \quad \mathbf{t}_z \equiv f'(z)\mathbf{e}_r + \mathbf{e}_z/\Lambda, \tag{2), (3}$$

where $(\mathbf{e}_r, \mathbf{e}_\theta, \mathbf{e}_z)$ are the unit vectors in the cylindrical coordinate system, and $\Lambda \equiv R/H$ is the aspect ratio.

The equations of motion and continuity are put in dimensionless form by scaling the radial and angular velocities $(u(r, z), v(r, z))$ with ΩR, the axial velocity $w(r, z)$ with ΩH, and the dynamic contribution to the pressure $p(r, z)$ with $\mu\Omega$, were μ is the fluid viscosity. The dimensionless equations are

$$Re\left(uu_r + wu_z - \frac{v^2}{r}\right) + \frac{p_r}{\Lambda} - \Lambda u_{zz} - \left(u_{rr} + \frac{u_r}{r} - \frac{u^2}{r}\right)\frac{1}{\Lambda} = 0, \tag{4a}$$

$$R_e\left(uv_r+wv_z+\frac{uv}{r}\right)-\Lambda v_{zz}-\left(v_{rr}+\frac{v_r}{r}-\frac{v^2}{r}\right)\frac{1}{\Lambda}=0, \tag{4b}$$

$$R_e(uw_r+ww_z)+\Lambda p_z-\Lambda w_{zz}-\left(w_{rr}+\frac{w_r}{r}\right)\frac{1}{\Lambda}=0, \tag{4c}$$

$$\frac{u}{r}+u_r+w_z=0, \tag{5}$$

where the subscripts on (u, v, w, p) denote partial differentiation, i.e. $u_r \equiv \partial u/\partial r$. The Reynolds number is defined by $R_e \equiv \Omega R H\rho/\mu$, and ρ is the density of the liquid. The boundary conditions appropriate to solving (4) and (5) are as follows: at the centreline $(r = 0,\ 0 \leqslant z \leqslant 1)$

$$u=0, \quad v=0, \quad \frac{\partial w}{\partial r}=0, \tag{6}$$

and at the surface of the disks $(0 \leqslant r \leqslant 1)$

$$u=0, \quad v=r, \quad w=0, \quad z=0, \tag{7}$$

$$u=0, \quad v=sr, \quad w=0, \quad z=1. \tag{8}$$

Equation (6) states the standard symmetry conditions for the centreline and (7) and (8) specify no slip and no penetration along the solid disks. The condition for no normal velocity at the meniscus $(r = f(z),\ 0 \leqslant z \leqslant 1)$ is

$$u-\Lambda f'(z)\,w=0, \tag{9}$$

and the balances of the tangential components of stress there are

$$T_{r\theta}-\Lambda f'(z)\,T_{z\theta}=0, \tag{10}$$

$$\Lambda f'(z)\,(T_{rr}-T_{zz})+(1-\Lambda^2 f'^2(z))\,T_{rz}=0, \tag{11}$$

when the drop is surrounded by a tenuous fluid. In these conditions $T_{r\theta}$, $T_{z\theta}$ etc. are components of the dimensionless stress tensor $\mathbf{T}$.

The balance of normal stress at the meniscus yields an equation for the interface shape:

$$C\mathbf{nn}:\mathbf{T}-\mathscr{P}-2\mathscr{H}=0, \tag{12}$$

where $2\mathscr{H}$ is the mean curvature of the meniscus:

$$2\mathscr{H} \equiv \frac{\Lambda^2 f(z) f''(z)-\Lambda^2 f'^2(z)-1}{(1+\Lambda^2 f'^2(z))^{\frac{3}{2}}}. \tag{13}$$

The capillary number $C \equiv \mu\Omega R/\sigma$ sets the relative importance of normal viscous stresses and surface tension σ in determining the shape of the meniscus, and so is the parameter that dictates the strength of the coupling between the flow field and the meniscus. The reference pressure difference $\mathscr{P}$ between the drop and the surrounding gas is scaled with σ/R and is determined so that any change in the drop shape conserves the volume as

$$\int_0^1 f^2(z)\,dz=1. \tag{14}$$

For molten semiconductors and many other liquids the capillary number is small; for example, a value of $C = 10^{-2}$ is large for a small-scale floating-zone system operating with either silicon or germanium, both of which have extremely high surface tensions. The weakness of the coupling between the change in meniscus shape caused by flow suggests a perturbation solution in powers of capillary number. To

do this for the free-boundary problem (4)–(14) we first transform the problem to a fixed cylindrical domain by introducing the mapping

$$x \equiv \frac{r}{f(z)} \quad (0 \leqslant x \leqslant 1). \tag{15}$$

Each variable is expanded in a Taylor series about $C = 0$ *as*

$$\begin{pmatrix} \mathbf{v}(x,z) \\ p(x,z) \\ f(z) \\ \mathscr{P} \end{pmatrix} = \begin{pmatrix} \mathbf{v}^{[0]}(x,z) \\ p^{[0]}(x,z) \\ f^{[0]}(z) \\ \mathscr{P}^{[0]} \end{pmatrix} + C \begin{pmatrix} \mathbf{v}^{[1]}(x,z) \\ p^{[1]}(x,z) \\ f^{[1]}(z) \\ \mathscr{P}^{[1]} \end{pmatrix}, \tag{16}$$

where $\mathbf{v} \equiv (u, v, w)^{\mathrm{T}}$. The selection of the cylindrical meniscus ($f^{[0]} = 1$, $\mathscr{P}^{[0]} = 1$) as the base state leads to a sequence of problems involving standard cylindrical coordinates with $x = r$. The flow field ($\mathbf{v}^{[0]}$, $p^{[0]}$) is calculated in §3. At higher orders, the normal-stress condition (12) is distinguished for calculating the correction to the meniscus shape caused by lower-order flow fields, and this shape correction then enters into the relations that determine the flow. This approach to the free-boundary problem is the essence of the technique of domain perturbations (Joseph 1973).

3. Flow structure at zero capillary number

The flow problem for the variables ($\mathbf{v}^{[0]}$, $p^{[0]}$) at zero capillary number is still nonlinear because of the inertial terms in the momentum equations (4). In the limit of zero Reynolds number these equations describe the simple shear flow

$$\mathbf{v}^{(0)} = (0, x(1+z(s-1)), 0), \tag{17a}$$

$$p^{(0)} = 0. \tag{17b}$$

We expand the field variables ($\mathbf{v}^{[0]}$, $p^{[0]}$) in Reynolds number about the flow (17) as

$$\mathbf{v}^{[0]} = \mathbf{v}^{(0)} + \mathbf{v}^{(1)} R_{\mathrm{e}} + O(R_{\mathrm{e}}^2), \quad p^{[0]} = p^{(0)} + p^{(1)} R_{\mathrm{e}} + O(R_{\mathrm{e}}^2), \tag{18}$$

and calculate the correction ($\mathbf{v}^{(1)}$, $p^{(1)}$) to the flow caused by inertia. It is simply shown that the equation and boundary conditions governing the angular component of velocity are homogeneous, and so $v^{(1)} = 0$.

The axial and radial components of velocity are sought in terms of the stream function $\psi^{(1)}(x, z)$ defined by

$$u^{(1)} \equiv \frac{1}{x}\frac{\partial \psi^{(1)}}{\partial z}, \quad w^{(1)} \equiv -\frac{1}{x}\frac{\partial \psi^{(1)}}{\partial x}. \tag{19}$$

The axial and radial momentum equations reduce to

$$D^4 \psi = -2\Lambda(s-1)x^2(1+z(s-1)), \tag{20}$$

with

$$D^2 \equiv \Lambda \frac{\partial^2}{\partial z^2} + \frac{1}{\Lambda}\left(\frac{\partial}{\partial x^2} - \frac{1}{x}\frac{\partial}{\partial x}\right). \tag{21}$$

The boundary conditions on $\psi^{(1)}(x, z)$ are derived from (6)–(11) as

$$\psi^{(1)} = \frac{\partial \psi^{(1)}}{\partial z} = 0 \quad (z = 0, 1; \quad 0 \leqslant x \leqslant 1), \tag{22}$$

$$\psi^{(1)} = D^2 \psi^{(1)} = 0 \quad (x = 0, 1; \quad 0 \leqslant z \leqslant 1). \tag{23}$$

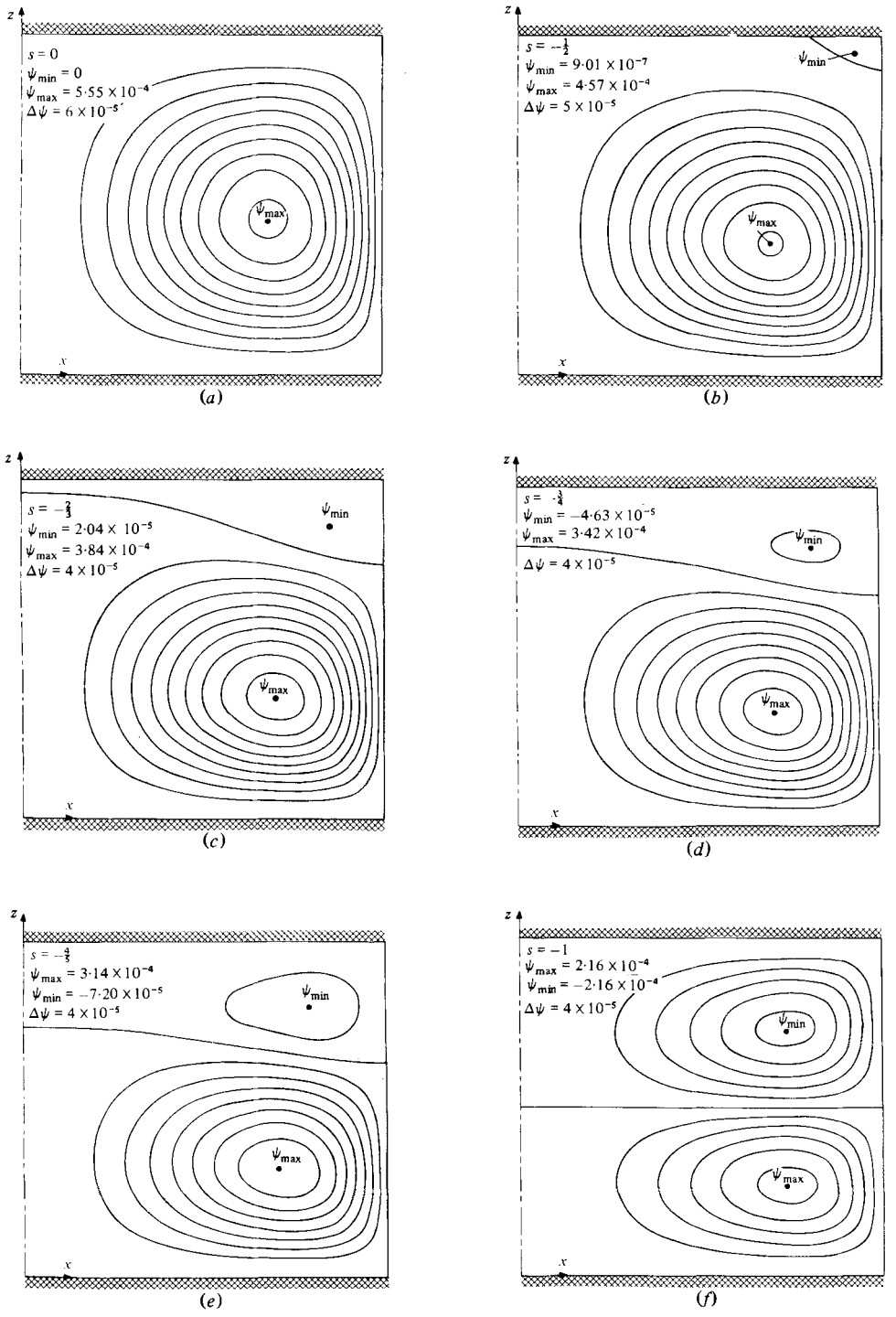

FIGURE 2. Streamlines for the inertially driven secondary flows in a drop with aspect ratio $\Lambda = 1$ and rotation ratios between 0 and -1.

The solution of (20)–(23) is

$$\psi^{(1)}(x,z) = 4(s-1)\Lambda^3 \sum_{p=1}^{\infty} \frac{xJ_1(k_p x)}{k_p^5 J_0(k_p)} H_p(z), \tag{24}$$

$$H_p(z) = 1+z(s-1)+(a_1+a_2 z)\sinh\frac{zk_p}{\Lambda}-(1+a_3 z)\cosh\frac{zk_p}{\Lambda} \tag{25}$$

and the eigenvalues $\{k_p\}$ are the roots of $J_1(k_p) = 0$. The constants (a_1, a_2, a_3) are defined in terms of $K \equiv k_p/\Lambda$ as

$$a_1 \equiv \frac{(\sinh K - sK)(1-\cosh K)}{K^2-\sinh^2 K}, \tag{26a}$$

$$a_2 \equiv \frac{sK^2 \sinh K+(\cosh K-1)[(1-s)\sinh K-K(s+\cosh K)]}{K^2-\sinh^2 K}, \tag{26b}$$

$$a_3 \equiv s-1+\frac{K(\sinh K-sK)(1-\cosh K)}{K^2-\sinh^2 K}. \tag{26c}$$

Generally the series (24) converges rapidly owing to the factor of k_p^{-5}, and as few as ten terms may be needed to resolve $\psi^{(1)}$ to within 1 % accuracy. More terms are needed near the axial boundaries and for zones with large aspect ratio.

The correction to the pressure field $p^{(1)}(x, z)$ is found by integrating the axial and radial momentum equations:

$$p^{(1)}(x,z) = \tfrac{1}{2}x^2-4\Lambda^3(s-1)\sum_{p=1}^{\infty}\frac{J_0(k_p x)}{k_p^4 J_0(k_p)}\left\{\frac{dH_p}{dz}-\left(\frac{k_p}{\Lambda}\right)^2\int_0^z H_p(y)\,dy\right\}. \tag{27}$$

The pattern of the correction to the flow $\psi^{(1)}$ caused by inertia is shown in figure 2, where the rotation ratio s is varied between 0 and -1 for a drop with unit aspect ratio. When the rotation ratio is positive a single toroidal cell exists like the one shown in figure 2 (*a*) for $s = 0$. Fluid is thrown radially outward near the lower rotating disk, moves along the meniscus, turns inward along the upper stationary surface and flows downward near the centreline to complete the cell. The cell weakens as the rotation ratio approaches unity, where the fluid moves in rigid-body rotation, as is easily seen by examining (24) and (27). In this limit the pressure field (27) is entirely centripetal.

When the top surface is counter-rotated ($s < 0$) a plane of zero angular velocity exists inside the drop (see (17)) and a new counter-circulating toroidal cell may form. As shown in figures 2 (*b–f*), this cell grows from the corner where the meniscus meets the upper disk, and spreads and intensifies as s approaches -1. For exact counter-rotation ($s = -1$), the flow field is separated precisely into two toroidal cells of the same strength and opposing circulation. Only in this limit do the surfaces of zero angular and axial velocity coincide.

When the aspect ratio is either small or large, simpler forms of $\psi^{(1)}(x, z)$ exist for describing the flow. In drops of small aspect ratio, the radial derivatives dominate (20) and (21), and $\psi^{(1)}(x, z)$ is well approximated away from the disks as

$$\psi^{(1)}(x,z) \approx -\tfrac{1}{96}\Lambda^3(s-1)(1+z(s-1))x^2(x^2-1)(x^2-2). \tag{28}$$

A simple characterization of the cellular flow is given by the streamline that divides the counter-circulating cells. From (28) this streamline occurs on the plane $z^* = (1-s)^{-1}$ and corresponds precisely to the plane of zero angular velocity.

When the streamline approaches to within $O(\Lambda)$ of the solid surface at $z = 1$, (28) is no longer valid because all derivatives in (21) are of comparable magnitude. The turning flows near the disks are clearly seen in the streamlines computed from the

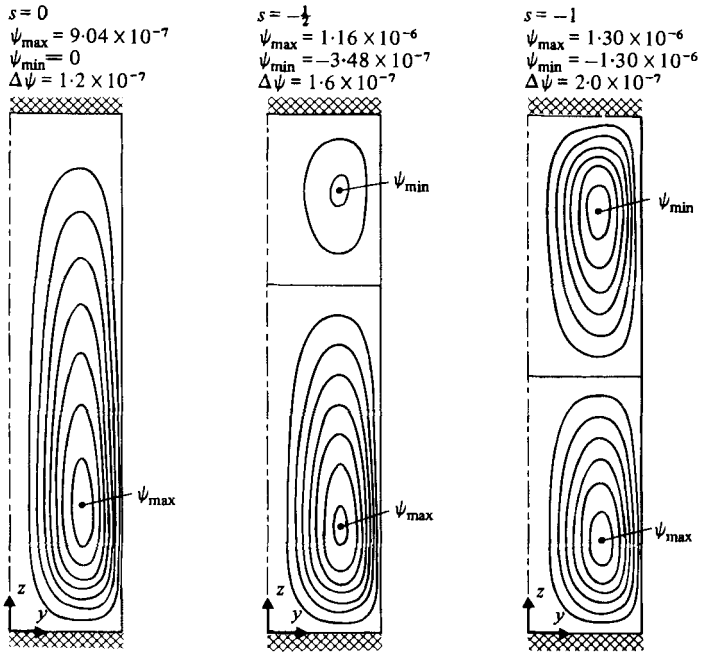

FIGURE 3. Streamlines for the inertially driven secondary flows in a drop with $\Lambda = \frac{1}{5}$ and s between 0 and -1. The radial coordinate has been stretched by the transformation $y \equiv \Lambda x$.

series solution (24) that are shown in figure 3 for $\Lambda = \frac{1}{5}$. The flow in this region is analysed by writing the full solution (25) near $z = 1$ as

$$H_p(z) \approx 1 + z(s-1) - \left[zs - (z-1)\left(1 + \frac{sk_p}{\Lambda}\right)\right] e^{(z-1)k_p/\Lambda} + O(e^{-k_p/\Lambda}). \tag{29}$$

The radial growth of the second cell is followed by expansion of the exponential term about $z = 1$ as

$$\psi^{(1)}(x,z) \approx 4\Lambda^2(s-1)(z-1)^2 \sum_{p=1}^{\infty} \frac{xJ_1(k_p x)}{k_p^4 J_0(k_p)} \left\{1 + \frac{sk_p}{2\Lambda} - s - \frac{sk_p}{2\Lambda}(z-1) + O(z-1)^2\right\}. \tag{30}$$

The disappearance of the second cell is marked by the value of s where the stagnation streamline coincides with the boundary at $z = 1$. From (30) this requires that

$$0 = \sum_{p=1}^{\infty} \frac{xJ_1(k_p x)}{k_p^4 J_0(k_p)} \left(1 - s + \frac{sk_p}{\Lambda}\right). \tag{31}$$

Additional expansions about $x = 0$ and $x = 1$ show that the upper cell first appears at the meniscus for

$$s = \frac{\Lambda}{\Lambda - 2{\cdot}725}, \tag{32}$$

and reaches the axis of rotation at

$$s = \frac{\Lambda}{\Lambda - 1{\cdot}678}. \tag{33}$$

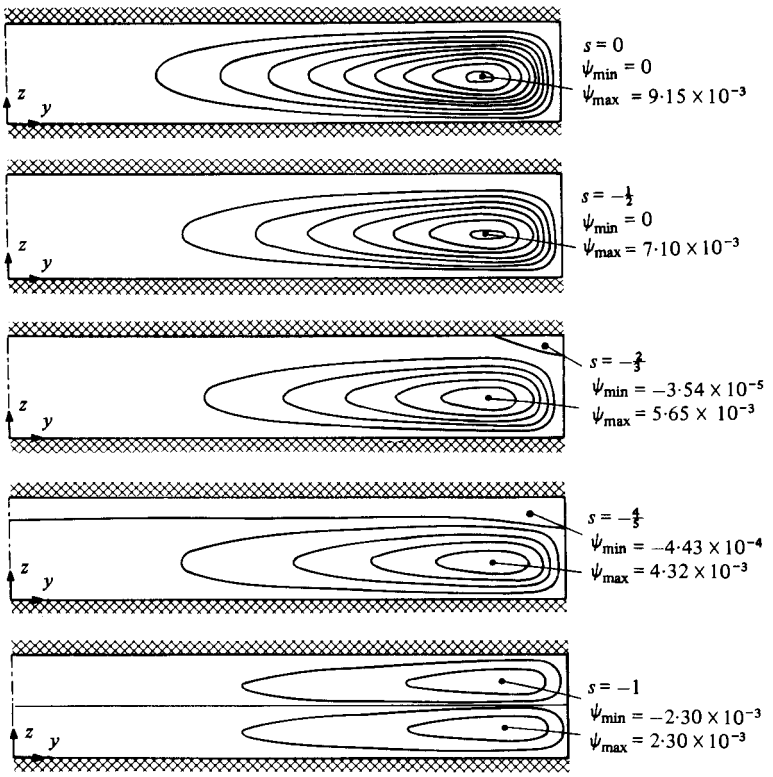

FIGURE 4. Streamlines for the inertially driven secondary flows in a drop with $\Lambda = 5$ and s between 0 and -1. The radial coordinate has been stretched by the transformation $y = \Lambda x$. The space between streamlines is $\Delta\psi = 1 \times 10^{-3}$ in each plot.

When the aspect ratio is large the axial derivatives dominate (20) and (21), and $\psi^{(1)}(x, z)$ is approximated in the core of the drop as

$$\psi^{(1)}(x,z) \approx \frac{-(s-1)x^2z^2(z-1)^2(z(s-1)+2s+3)}{60\Lambda}, \tag{34}$$

This form of the stream function is the generalization of the result of Schultz-Grunow (1935) for the low-Reynolds-number flow in the core between stationary and rotating disks of large radius and is a similarity solution (Kármán 1921) for this case. In fact, the core flows in both geometric extremes of large and small aspect ratio are similarity forms where the velocity parallel to the shortest dimension is independent of the long coordinate.

When two cells form, the axial location of the dividing streamline is at $z = (2s+3)/(1-s)$, which exists for rotation ratios in the range

$$-1 \leqslant s \leqslant -\tfrac{2}{3}. \tag{35}$$

The expression (34) is not valid within $O(1/\Lambda)$ of the meniscus because of the turning flow near the meniscus. Joseph (1975) used the form (34) as an outer solution in a singular perturbation expansion for determining the flow near the meniscus in terms of a series of the complicated Papkovich–Fadle eigenfunctions. Of course, this turning flow is readily found from the series of Bessel functions given by (24); representative secondary flows are shown in figure 4 for $\Lambda = 5{\cdot}0$.

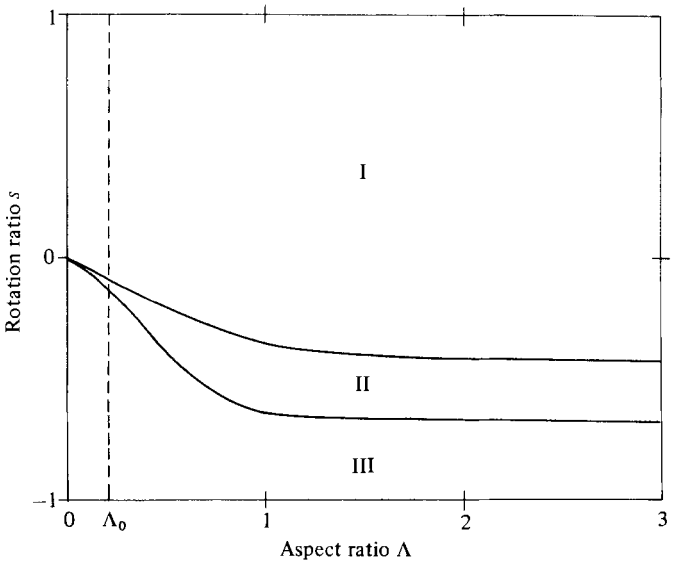

FIGURE 5. Phase diagram of flow structure as a function of aspect ratio Λ and rotation ratio s.

The dependence of the flow structure on the aspect and rotation ratios is shown on figure 5, which is composed of asymptotic results for large and small aspect ratios connected by computations of the stagnation streamline from the series solution (24). The cellular flows are classified as either:

(I) a single toroidal cell;

(II) two cells, one not extending to the axis of rotation;

(III) two cells, both reaching the axis of rotation.

The entire range of aspect ratio is shown, although the drop becomes unstable at Λ less than $1/2\pi$, the Plateau–Rayleigh limit.

4. Meniscus deformations at low capillary numbers

The deflections of the meniscus from the cylindrical form caused by the inertially driven flows described in §3 are governed by the linearized form of the normal stress balance,

$$\left(\Lambda^2 \frac{d^2}{dz^2}+1\right) f^{[1]}(z)+\mathscr{P}^{[1]} = \left(2\frac{\partial u^{[0]}}{\partial x}-p^{[0]}\right)_{x=1}, \tag{36}$$

by the volume constraint,

$$\int_0^1 f^{[1]}(z)\,dz = 0, \tag{37}$$

and by the pinning conditions along the perimeter of the disks

$$f^{[1]}(1) = f^{[1]}(0) = 0. \tag{38}$$

When the aspect ratio is not near the Plateau–Rayleigh limit of $1/2\pi$, the solution of (36)–(38) is straightforward and yields

$$\left.\begin{aligned} f^{[1]}(z) &= 4(s-1)\Lambda^3 R_e\left(\alpha_1+\alpha_2 \sin\frac{z}{\Lambda}+\alpha_3\cos\frac{z}{\Lambda}+\phi(z)\right), \\ \mathscr{P}^{[1]} &= -\tfrac{1}{2}-4(s-1)\Lambda^3 R_e\alpha_1, \end{aligned}\right\} \tag{39}$$

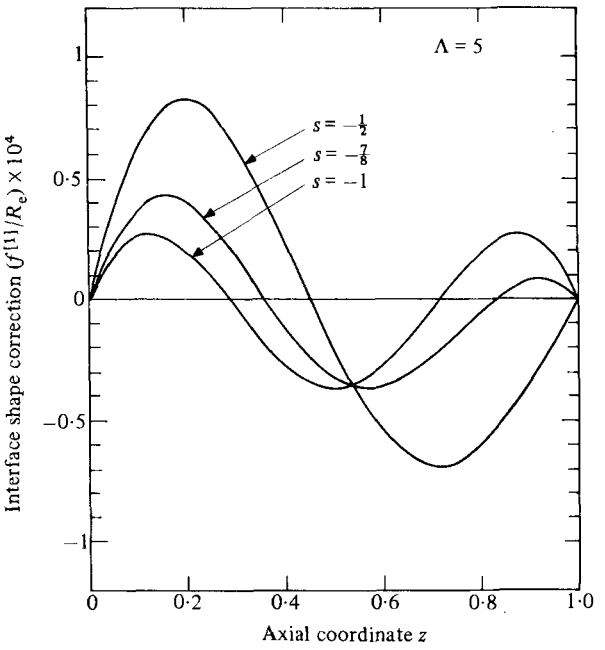

FIGURE 6. Meniscus deflections for drops with aspect ratio $\Lambda = 5$ and rotation ratios s of $-\frac{1}{2}$, $-\frac{7}{8}$ and -1.

where

$$\phi(z) = \frac{(s-1)(9\Lambda^2-4z^2)-8z}{64\Lambda^2} + 2\sum_{p=1}^{\infty}\left\{\frac{dH_p}{dz}-(s-1)\right.$$
$$\left.+\frac{1-k_p^2}{1+k_p^2}\left(a_2\sinh\frac{zk_p}{\Lambda}+a_3\cosh\frac{zk_p}{\Lambda}\right)\right\}\Big/k_p^4(1+k_p^2), \qquad (40)$$

and the constants $(\alpha_1, \alpha_2, \alpha_3)$ are

$$\left.\begin{aligned}
\alpha_1 &\equiv \frac{-\Lambda(1-\cos(1/\Lambda))(\phi(0)+\phi(1))+\sin(1/\Lambda)\,\Phi}{2\Lambda(1-\cos(1/\Lambda))-\sin(1/\Lambda)},\\
\alpha_2 &\equiv \frac{(1-\cos(1/\Lambda))(\phi(0)-\Phi)-(1-\Lambda\sin(1/\Lambda))(\phi(0)-\phi(1))}{2\Lambda(1-\cos(1/\Lambda))-\sin(1/\Lambda)},\\
\alpha_3 &\equiv \frac{\sin(1/\Lambda)(\phi(0)-\Phi)-\Lambda(1-\cos(1/\Lambda))(\phi(0)-\phi(1))}{2\Lambda(1-\cos(1/\Lambda))-\sin(1/\Lambda)},
\end{aligned}\right\} \qquad (41)$$

with $\Phi \equiv \int_0^1 \phi(z)\,dz$. Representative shape corrections are shown in figures 6–8 for aspect ratios of 5, 1 and $\frac{1}{5}$. The deflection of the meniscus is reflectively symmetric about the midplane of the drop for exact counter-rotation, and bulges outward more near the faster spinning disk for other values of s. The magnitude of the deflection decreases as $O(\Lambda^{-2})$ when the aspect ratio of the drop becomes large.

When the aspect ratio approaches $1/2\pi$ the correction to the meniscus shape (39) becomes unbounded unless $\phi(0) = \phi(1)$. This condition is only met when the normal stress acting on the meniscus is reflectively symmetric, as for $s = \pm 1$. In the case of iso-rotation ($s = 1$), the meniscus remains cylindrical. For exact counter-rotation ($s = -1$) at $\Lambda = 1/2\pi$, the constants (α_1, α_3) are

$$\alpha_1 \equiv \Phi, \quad \alpha_3 \equiv -\phi(0)+\Phi, \qquad (42)$$

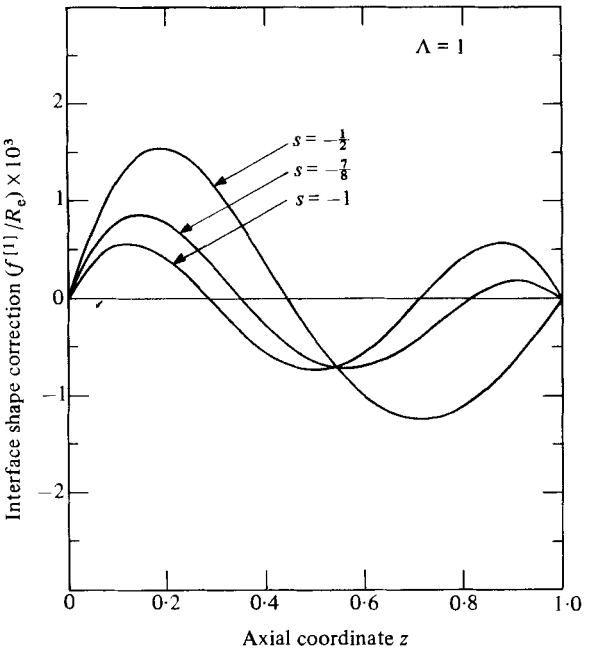

FIGURE 7. Meniscus deflections for drop with $\Lambda = 1$.

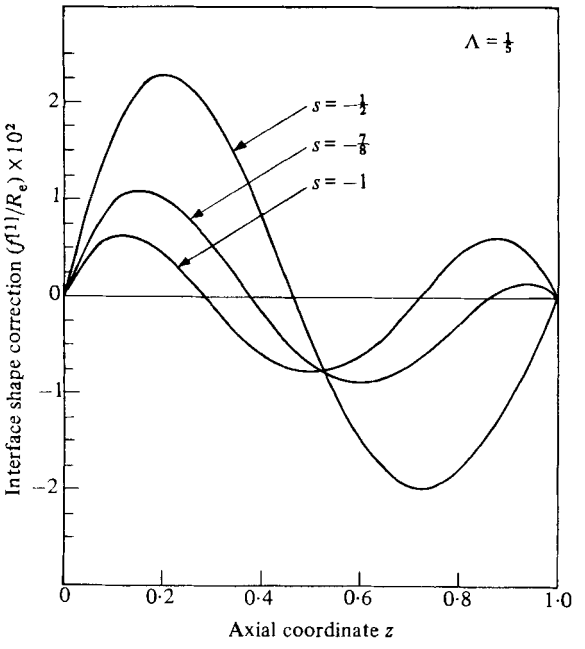

FIGURE 8. Meniscus deflections for drop with $\Lambda = \frac{1}{5}$.

and α_2 is not determined solely from the problem at first order in C. The regular perturbation (16) in capillary number fails when the rotation ratio s is not ± 1. The significance of this behaviour is readily explained by examining the coupling between the flow field and the multiple static meniscus shapes that exist near the Plateau–Rayleigh limit.

4.1. $C = 0$: *perfect bifurcation*

The unduloidal shapes that evolve from the cylindrical drop at the Plateau–Rayleigh limit are captured by standard perturbation techniques for analysing bifurcations Iooss & Joseph 1980). Following the methodology in Brown & Scriven (1980), the drop shape, reference pressure and aspect ratio are expanded as a Taylor series in an amplitude parameter ϵ that measures the difference between the cylindrical menisci and the bifurcating forms:

$$\begin{pmatrix} f(z;\epsilon) \\ \mathscr{P}(\epsilon) \\ \Lambda(\epsilon) \end{pmatrix} = \sum_{n=0}^{\infty} \frac{\epsilon^n}{n!} \begin{pmatrix} f_n(z) \\ \mathscr{P}_n \\ \Lambda_n \end{pmatrix}. \tag{43}$$

The scaling ϵ serves but one purpose; it provides a systematic means of determining the proper relation between the magnitude of the shapes in the bifurcating family and the distance (in aspect ratio) from the point of bifurcation. Once a non-zero term of higher order is found in the expansion for aspect ratio this series is inverted to yield an explicit relationship between ϵ and $\Lambda - \Lambda_0$.

The $O(\epsilon)$ terms in (43) are governed by the homogeneous versions of (36)–(38), which are solved as an eigenvalue problem for a set of eigenvalues Λ_0 and eigenfunctions $(f_1, \mathscr{P}_1)$. These values of Λ_0 mark the bifurcation of families of unduloidal shapes from the cylinder. The largest one, $\Lambda_0 \equiv 1/2\pi$, is the Plateau–Rayleigh limit, and we focus only on this bifurcation. To leading order in amplitude the drop shape and reference pressure along this new shape family are

$$f(z) = 1 \pm A(\Lambda) \sin 2\pi z + O(A^2), \tag{44a}$$

$$\mathscr{P} = 1 + \tfrac{1}{2}A^2 + O(A^4), \tag{44b}$$

where the amplitude $A(\Lambda)$ is defined as

$$A(\Lambda) \equiv (\tfrac{8}{3}\pi)^{\frac{1}{2}} (\Lambda - 1/2\pi)^{\frac{1}{2}}. \tag{44c}$$

These unduloidal shapes bifurcate supercritically in terms of Λ from the cylindrical family at $\Lambda = 1/2\pi$ and are unstable (Ungar & Brown 1982). Both shape families are represented on the bifurcation diagram figure 9, where the amplitude of the difference between the unduloidal and cylindrical shape is plotted against the aspect ratio.

4.2. $C \neq 0$: *imperfect bifurcation*

For aspect ratios near $1/2\pi$, the Taylor series (16) in capillary number is not unique, and the equations for meniscus shapes (36)–(38) are singular, reflecting this multiplicity. The unbounded solution (39) for $\Lambda \equiv \Lambda_0 = 1/2\pi$ is symptomatic of a singular dependence of the bifurcation on C, and points to a rescaling of the dependence of aspect ratio with C along the solution families. We determine this scaling by the singular perturbation technique developed by Matkowsky & Reiss (1977). Once more, the variables $(f(z), \mathscr{P}, \Lambda, C)$ are expanded in a Taylor series in a new scaling parameter. The relationship between this parameter, the aspect ratio and

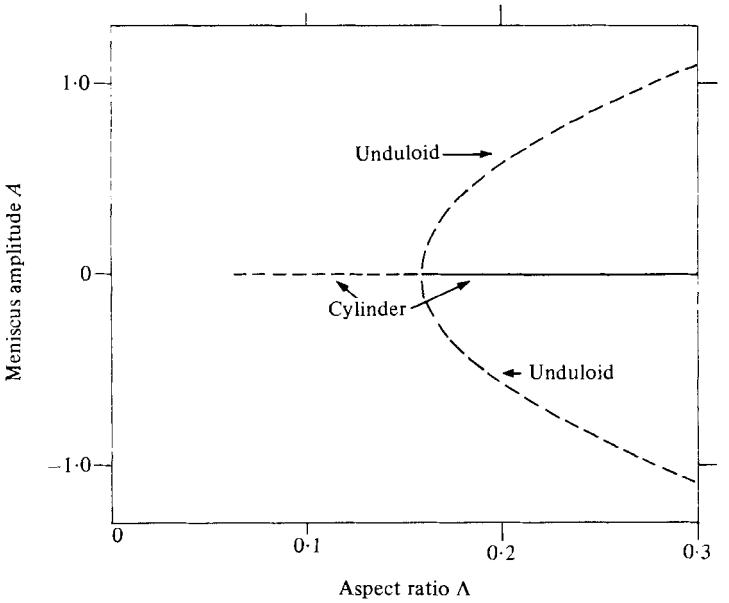

FIGURE 9. Plot of amplitude of the meniscus deflection versus aspect ratio for static meniscus shapes; $C = 0$. The Plateau–Rayleigh limit is $\Lambda \equiv \Lambda_0 = 1/2\pi$. Solid lines denote stable shapes and dashed lines unstable ones.

the capillary number is determined so that bounded solutions for the shape and pressure are found near $\Lambda = 1/2\pi$. The details of this application to the differentially rotated captive drop are similar to the analysis presented in Ungar & Brown (1982) and are not repeated here.

The appropriate scaling between Λ and C close to the Plateau–Rayleigh limit is given by the inner parameter

$$\eta \equiv \frac{\Lambda - \Lambda_0}{C^{\frac{2}{3}}}, \tag{45}$$

and the corresponding form of the shape correction is

$$f(z) = 1 + C^{\frac{1}{3}} A(\eta) \sin 2\pi z + O(C^{\frac{2}{3}}). \tag{46}$$

The amplitude of the correction is defined by the cubic equation

$$A^3 - \tfrac{8}{3}\pi\eta A - \frac{(s^2-1)R_e}{12\pi^2}\left(1 + \frac{16\beta}{\pi}\right) = 0, \tag{47}$$

with

$$\beta \equiv \sum_{p=1}^{\infty} \frac{k_p^2 - 1}{k_p^3(k_p^2+1)^2}\left(\frac{\cosh 2\pi k_p - 1}{2\pi k_p + \sinh 2\pi k_p}\right) \approx 9{\cdot}96 \times 10^{-3}. \tag{48}$$

The amplitude of the inner solution is plotted on figure 10 for selected values of $\mathscr{B} \equiv R_e(1-s^2)$. For $\mathscr{B} \neq 0$, the bifurcation is ruptured by the normal stress into two distinct curves. Loss of stability of the slightly distorted drops now occurs at the limit point where two solutions of (47) merge (Matkowsky & Reiss 1977). The value of Λ for this limit point is given by the condition for the vanishing of the discriminant of (47):

$$\Lambda^* = \tfrac{1}{2}\pi\{1 + 0{\cdot}028 C^{\frac{2}{3}} R_e^{\frac{2}{3}}(s^2-1)^{\frac{2}{3}} + \ldots\}. \tag{49}$$

An analytical expression for the stable drop shape that is uniformly valid in Λ is found

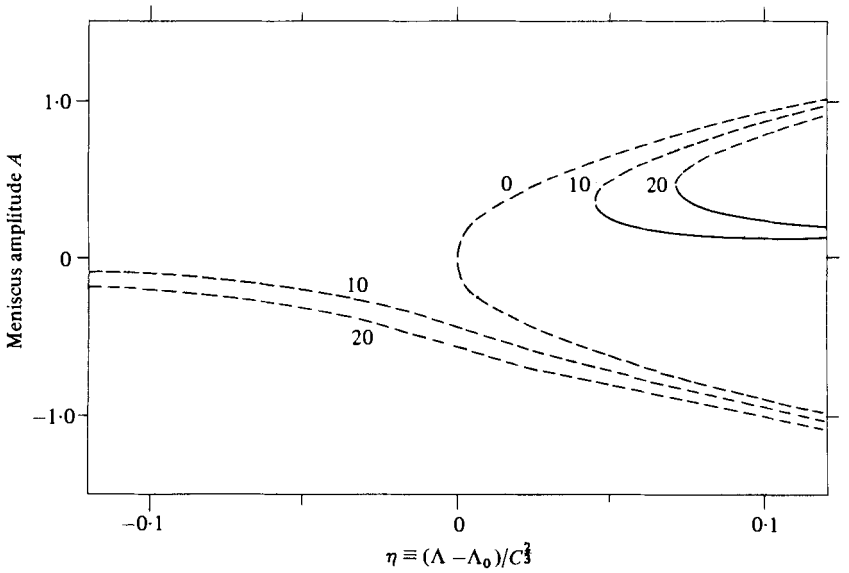

FIGURE 10. Effect of secondary flows on the Plateau–Rayleigh stability limit is shown as a plot of the amplitude of the meniscus deflection as a function of aspect ratio. Curves are for fixed values of $\mathscr{B}$.

by matching the inner solution (46) with the outer solution given by (39)–(41), as outlined in Matkowsky & Reiss (1977). The inner limit of the outer solution is

$$f(z) \approx 1 - \frac{C^{\frac{1}{3}} R_e (s^2-1)\,(1+16\beta/\pi)}{32\eta\pi^3} \sin 2\pi z. \tag{50}$$

Accordingly, the inner amplitude that matches with (50) in the outer limit is

$$A(\eta) = \tfrac{4}{3}(2\pi\eta)^{\frac{1}{2}} \cos\left(\tfrac{1}{3}\theta + \tfrac{4}{3}\pi\right), \tag{51}$$

where

$$\theta = \arccos\left\{\frac{9R_e(s^2-1)}{128\pi^3(2\pi)^{\frac{1}{2}}}\left(1+\frac{16\beta}{\pi}\right)\eta^{-\frac{3}{2}}\right\}.$$

For exact counter-rotation, $\mathscr{B} = 0$ and the bifurcation is not broken. In this case the expansion in capillary number is regular and the first-order flow field ($\mathbf{v}^{[1]}$, $p^{[1]}$) couples into the condition for the solvability of the normal stress balance at second order in C. The shape constant α_2 is determined by this condition. The bifurcation point will shift to a larger aspect ratio; the calculation of the shifting requires the computation of the correction to the flow field caused by the meniscus deflection, and is not presented here.

5. Discussion

The structure of the cellular motions in cylindrical drops is completely determined for low Reynolds numbers by the asymptotic analysis described here. The most significant results for the floating-zone method of crystal growth are the forms of the velocity field near the disks, either of which may represent the growing crystal. Except at high aspect ratio, the turning flows near the centre of the crystal and the meniscus cover significant portions of the solidification front and lead to appreciable radial segregation of solutes in the crystal for any value of the rotation ratio away from

unity. The specific form of the radial concentration profile in the crystal depends on the value of s and on whether the crystal grows from the upper or lower surface. The type II flows are of particular interest when the second toroidal cell separates along the solidification interface, because the presence of this stagnation curve will lead to an annulus of sharp variation of composition within the crystal. The ranges of s and Λ for types II flows are given on figure 5.

Experimental verification of the shapes of the cells predicted here is complicated by the much faster azimuthal motion on which these secondary flows are superimposed. Fowle *et al.* (1980) used particle-tracking methods to detect the point on the meniscus where the angular velocity vanished, and tried to infer the structure of the secondary motions solely from this result. For aspect ratios near unity, this conclusion is not possible because the plane of vanishing angular velocity predicted from (17) is not the same as the curve of the streamline dividing the two cells.

The extent of validity of the results given here rigorously is limited to small Reynolds number, but can be expanded systematically by considering the next terms in the Taylor series (18). Then the first non-zero correction to the azimuthal velocity arises at $O(R_e^2)$ and the first corrections to u, w and p occur at $O(R_e^3)$. We choose not to calculate these corrections, but instead compare the asymptotic results with numerical solutions of the entire equations; these calculations will be presented elsewhere (Harriott & Brown 1982). The comparison for $\Lambda = 1{\cdot}0$ and $s = -1{\cdot}0$ shows the asymptotic solution to be within 10% of the numerical results for Reynolds numbers up to 50. This extended range of validity of a solution developed for low Reynolds numbers is similar to results that have been found for other confined rotating flows (Pao 1970).

Although the meniscus deflections caused by the flow are small for small capillary number (see figure 5), they have a pronounced effect on the structure of the solutions near the Plateau–Rayleigh limit $\Lambda_0 \equiv 1/2\pi$. The breaking of the shape families that exist for zero capillary number is understood in terms of the symmetries of the shapes at zero capillary number and the symmetries of the deflections caused by the flow. The shape families are broken whenever the deflection caused by the flow has any component with the same symmetry as the unduloid shapes that bifurcate at $C = 0$. This symmetry requirement prescribes the potential interactions between deflections of the meniscus shape caused by other either buoyancy-driven or surface-tension-driven flows with the Plateau–Rayleigh limit.

This research was supported by the Materials Processing Program of the U.S. National Aeronautic and Space Administration.

REFERENCES

Boucher, E. A. & Evans, M. J. B. 1980 Capillary phenomena XII. Properties of fluid bridges between solids in a gravitational field. *J. Colloid Interface Sci.* **75**, 409–418.

Brown, R. A. & Scriven, L. E. 1980 The shape and stability of rotating captive drops. *Phil. Trans. R. Soc. Lond.* A **297**, 51–79.

Burton, J. A., Prim, R. C. & Slichter, W. P. 1953 The distribution of solute in crystals grown from the melt. *J. Chem. Phys.* **21**, 1987–1991.

Carruthers, J. R. & Grasso, M. 1972 Studies of floating zones in simulated zero gravity. *J. Appl. Phys.* **43**, 436–443.

Cochran, W. G. 1934 The flow due to a rotating disk. *Proc. Camb. Phil. Soc.* **30**, 365–375.

CORIELL, S. R., HARDY, S. C. & CORDES, M. R. 1977 Stability of liquid zones. *J. Colloid Interface Sci.* **60**, 126–136.

FOWLE, A. A., SOTO, L., STRONG, P. F. & WANG, C. A. 1980 Experimental and flow characteristics of floating liquid columns confined between rotating disks. *Final report to NASA, Washington, D.C., Contract no.* NASW-3186 *by Arthur D. Little, Feb.* 1980.

GIBBS, J. W. 1906 In *Scientific Papers*, Vol. 1, Dover.

HARRIOTT, G. M. & BROWN, R. A. 1982 Flow in a differentially rotated cylindrical drop at moderate Reynolds number. (Unpublished manuscript.)

HEYWANG, W. VON 1956 Zur Stabilität senkrechter Schmelzzonen. *Z. Naturforschung* **11**a, 238–243.

IOOSS, G. & JOSEPH, D. D. 1980 *Elementary Stability and Bifurcation Theory*. Springer.

JOSEPH, D. D. 1973 Domain perturbations: the higher-order theory of infinitesimal water waves. *Arch. Rat. Mech. Anal.* **51**, 295–303.

JOSEPH, D. D. 1975 Slow motion and viscometric motion. *Arch. Rat. Mech. Anal.* **56**, 99–157.

KÁRMÁN, TH. VON 1921 Über laminare und turbulente Reibung. *Z. angew. Math. Mech.* **1**, 233–251.

KELLER, W. & MUHLBAUER, A. 1981 *Floating Zone Silicon*. Marcel-Dekker.

LAWAL, A. & BROWN, R. A. 1982 The stability of an inclined pendent drop. *J. Colloid Interface Sci.* (in press).

MASON, G. J. 1970 An experimental determination of the stable length of cylindrical liquid bubbles. *J. Colloid Interface Sci.* **32**, 172–176.

MATKOWSKY, B. J. & REISS, E. L. 1977 Singular perturbations of bifurcations. *SIAM J. Appl. Math.* **33**, 230–255.

PAO, H.-P. 1970 A numerical computation of a confined rotating flow. *J. Appl. Mech.* **37**, 480–487.

PFANN, W. G. 1966 *Zone Melting*, 2nd edn. Wiley.

PLATEAU, J. A. F. 1873 *Statique Expérimentale et Théorique des Liquides soumis aux seules forces moléculaires*. Gauthier-Villars.

RAYLEIGH, J. W. S. 1879 On the capillary phenomena of jets. *Proc. R. Soc. Lond.* **29**, 71–97.

SCHULTZ-GRUNOW, F. 1935 Der Reibungswiderstand rotierenden Scheiben in Gehäusen. *Z. angew. Math. Mech.* **15**, 191–204.

UNGAR, L. H. & BROWN, R. A. 1982 The dependence of the shape and stability of captive rotating drops on multiple parameters. *Phil. Trans. R. Soc. Lond.* (in the press).